



Lesgidis, N., Sextos, A., Moschen, L., Juan S., G. G., & Pistone, E. (2020). Rigorous vehicle soil track simulation of high speed rail through optimization based model order reduction. *Transportation Geotechnics*, 23, [100350].
<https://doi.org/10.1016/j.trgeo.2020.100350>

Peer reviewed version

License (if available):
CC BY-NC-ND

Link to published version (if available):
[10.1016/j.trgeo.2020.100350](https://doi.org/10.1016/j.trgeo.2020.100350)

[Link to publication record in Explore Bristol Research](#)
PDF-document

This is the author accepted manuscript (AAM). The final published version (version of record) is available online via Elsevier at <https://www.sciencedirect.com/science/article/pii/S2214391219303988>. Please refer to any applicable terms of use of the publisher.

University of Bristol - Explore Bristol Research

General rights

This document is made available in accordance with publisher policies. Please cite only the published version using the reference above. Full terms of use are available:
<http://www.bristol.ac.uk/red/research-policy/pure/user-guides/ebr-terms/>

Rigorous vehicle-soil-track simulation of high-speed rail through optimization-based model order reduction

Nikolaos Lesgidis^{1*}, Anastasios Sextos¹, Lukas Moschen², Gutierrez G. Juan S.², Elisabetta Pistone²

¹ Department of Civil Engineering, University of Bristol, United Kingdom

² Vienna Consulting Engineers ZT GmbH, Vienna, Austria

* Corresponding author

ABSTRACT

This paper aims to develop a time domain analysis method capable of accurately simulating the vehicle-soil-track interaction phenomenon in a computationally rigorous manner. The proposed method takes full account of wave propagation effects in the subsoil half-space through the development of a systematic frequency dependent lumped parameter assembly. A robust multi-objective optimization methodology is proposed for the calibration of the developed lumped parameter assembly targeting the dynamic behavior, global stability and passivity of the track-subsoil system while maintaining the broad applicability of the method by any commercial FEM software. A case study of a ballasted track on a soft clay profile is presented in order to investigate the efficiency of the proposed methodology. Finally, the monitored response of a modern ballastless high speed track located in mainland Europe is used for further verification. Results demonstrate the efficiency, accuracy and applicability of the proposed methodology.

Keywords: Track dynamics; Track-soil interaction; Vehicle-track interaction measurement; Railway vibration; Ground vibration

1. INTRODUCTION

Over the last decades, significant progress in the fields of construction, operating and maintaining of railway transportation facilities has led to the continuing increase of both the speed and the allowable carried load of railway trains. As a result, engineering decisions relating to design and maintenance of the high-speed railway substructure are affected by a set of different issues compared to the ones observed in conventional-speed railway. The accurate prediction of the vibration

induced by trains traveling at critical speeds is a mandatory requirement and recent topic of discussion for the design of state-of-the-art high-speed track-substructure systems [1]. Additionally, maintenance is not always straightforward in the aforementioned scenario due to potential damage in the subgrade, a challenging condition to diagnose and remedy [2]. As a result, a realistic representation of the subgrade system in a stochastic multivariable, yet computationally efficient, simulation environment can significantly aid during the design of a high-speed railway network and provide forecasting information during maintenance planning.

A vehicle-track-soil dynamic system is composed of subsystems of different natures and therefore it is common in literature to integrate the vehicle and track-subsoil segments separately by implicitly coupling different simulation techniques. The vehicle is typically modeled as a multi-body system in order to fully take into consideration both the interaction between substructures [3,4] of the vehicle (wheel, bogie, and passenger stage) and the interaction between the vehicle and the track [5–7]. Furthermore, for the track-soil subsystem additional requirements need to be fulfilled during the construction of a simulation model as an accurate simulation of wave propagation within the semi-infinite medium is of paramount importance in the study of high-speed train behavior. This is further reinforced by literature, where simplification on the coupling behavior induced by wave propagation in the soil domain has been illustrated to misrepresent the actual behavior of the soil-track system [8,9]. Subsequently, the popular frequency-independent and uncoupled Winkler model frequently used in literature is considered an obsolete approach for the study of high-speed railway behavior. Additionally, frequency domain-based methodologies previously proposed are limited to the simulation of viscous elastic behavior, a non-realistic assumption for rail pad and wheel-rail contact behavior.

Numerous approaches have been established in the past addressing the simulation of the detailed soil-track interaction subsystem in the time domain. The truncated simulation of the soil domain with silent boundaries by the finite element method (FEM) is an example of a direct approach where the behavior of wave propagation, reflection and refraction within the soil medium is maintained. As observed in literature, the direct FEM method has been frequently utilized in the simulation of track-soil systems [10–14]. Alternatively, a robust consideration of the semi-infinite subsoil half-space can be accomplished through the use of the coupled finite element boundary element method (FEM-BEM). Both 2.5D and 3D domain FEM-BEM solutions have been effectively used in the past in [15–17].

The main disadvantage of the truncated FEM and coupled BEM-FEM methods is the high computational cost associated with both methods. In the light of the above limitation, it is common to refine the subsoil domain size and subsequently reduce the analysis computational cost by reducing

the order of the system. Such a task can be accomplished through a partition approach of the overall dynamic system in segments, where the subsoil domain is significantly condensed on its internal degrees of freedom (DOF), while the remaining system is left unaltered. At this point it is important to state that an order reduction approach will limit the option of a direct prediction of ground vibration at an arbitrary location within the soil medium.

The lumped parameter (LP) method has been established as a popular and computationally viable alternative for the reduced simulation of soil structure interaction under earthquake induced vibrations [18–22]. The LP method has also illustrated promising results in the simulation of vehicle-track-soil dynamics. Low order LP models have been utilized in the past, capturing the single point semi-infinite track-soil behavior for the study of wheel-rail dynamic interaction [23], and a multiple point subsoil LP assembly in the time domain has been proposed in [24]. The proposed method provides a frequency dependent representation of the direct dynamic flexibility but neglects any coupling behavior of the subsoil system. An LP assembly considering both the direct and coupling behavior of the subsoil segment in a simplified manner has been recently proposed in [25] and used in [26] where the direct and coupling behaviors are roughly approximated by Kelvin-Voigt and enhanced Kelvin-Voigt models. Finally, a sophisticated LP methodology for the simulation of the subsoil domain has been recently proposed in [27]. However, even the most sophisticated LP methods implemented in the simulation of soil-track-vehicle interaction introduce a number of limitations. Most importantly, the properties of global stability and passivity [28] for the overall train-track system are not necessarily preserved. Both the stability and passivity of a targeted system are fundamental properties that are not necessarily maintained in an order reduction process. This is expected since the reduced system is only targeting the particular solution (steady state) of the original system in the form of dynamic flexibility functions and not the complementary solution (transient state). The aforementioned omission could potentially lead to an unstable complementary solution of the reduced ordinary differential equation system regardless of the external excitation. Furthermore, the use of the Routh–Hurwitz stability criterion as a constraint in the lumped parameter model calibration, a strategy adopted by a family of rational approximation models in the literature, does not necessarily lead to a stable overall system as mathematically and numerically proven in [21,29,30]. Secondly, the calibration process of the LP model is formulated as a multi-objective optimization problem with an infinite number of objective functions. The optimization problem is complex and the selection of an LP model variable combination even among the generated pareto front is not a trivial task.

To this end the original contribution of the paper is twofold, namely (a) the proposal of a globally stable and commercially applicable LP assembly procedure, capable of significantly

reducing the computational cost introduced by the soil-track interacting system and (b) the development of a robust and reliable optimization approach for the calibration of the proposed LP assembly. Regarding the first aspect, an infinite LP assembly is mathematically derived in accordance to the longitudinal periodicity of the isolated sleeper-ballast-soil (or slab-soil) system. The proposed LP assembly utilizes a proposed coupling LP component capable of capturing the fluctuations of the imaginary part of coupling receptance functions typically observed in soil-track systems, while maintaining global stability of the system. Regarding the second aspect, the authors present a robust optimization approach which exploits the importance of adjacent coupling between neighboring sleepers. The proposed optimization approach can select a reliable point along the pareto front in a consistent manner.

2. DYNAMIC MODEL ORDER REDUCTION

2.1 Methodology overview

Given the inability of existing modeling procedures to capture the frequency dependent vehicle-track-soil interaction in a computationally viable and reliable manner, the methodology for an optimization-based model order reduction of the soil-track system is proposed herein. The proposed procedure implements the reduced order simulation of a vehicle-track-soil system in different individual steps as illustrated in the flowchart of figure 1. In an initial step, segments of the overall system associated with high computational cost are highlighted. The selected segments are isolated from the remaining dynamic system and transformed in the frequency domain. In a second step, the transformed segments are significantly reduced through a dynamic condensation procedure. The order reduction procedure reformulates the isolated segment in the frequency domain representing the behavior of the isolated segment at its interface with the remaining dynamic system.

In a final step the condensed segment is transformed back to the time domain through a multi-objective optimization procedure. In more detail, a lumped parameter model defined as a parametric ordinary differential equation system is constructed in accordance with the morphology of the targeted condensed segment. The parameters of the lumped parameter model are calibrated with the goal of capturing the condensed system behavior in the frequency domain while maintaining fundamental properties of the targeted system such as passivity and stability. The reduced LP assembly and the remaining multi-body dynamics system are recombined in accordance with the interface regions defined during the partition step of the proposed procedure.

At this point it is important to state that the proposed procedure is formulated in accordance with an extraction of the dynamic flexibility functions of the track-soil system from a simulation model defined either through the finite element method or the hybrid finite element and

boundary element method. In the following paragraphs the formulation of the proposed methodology is presented in detail.

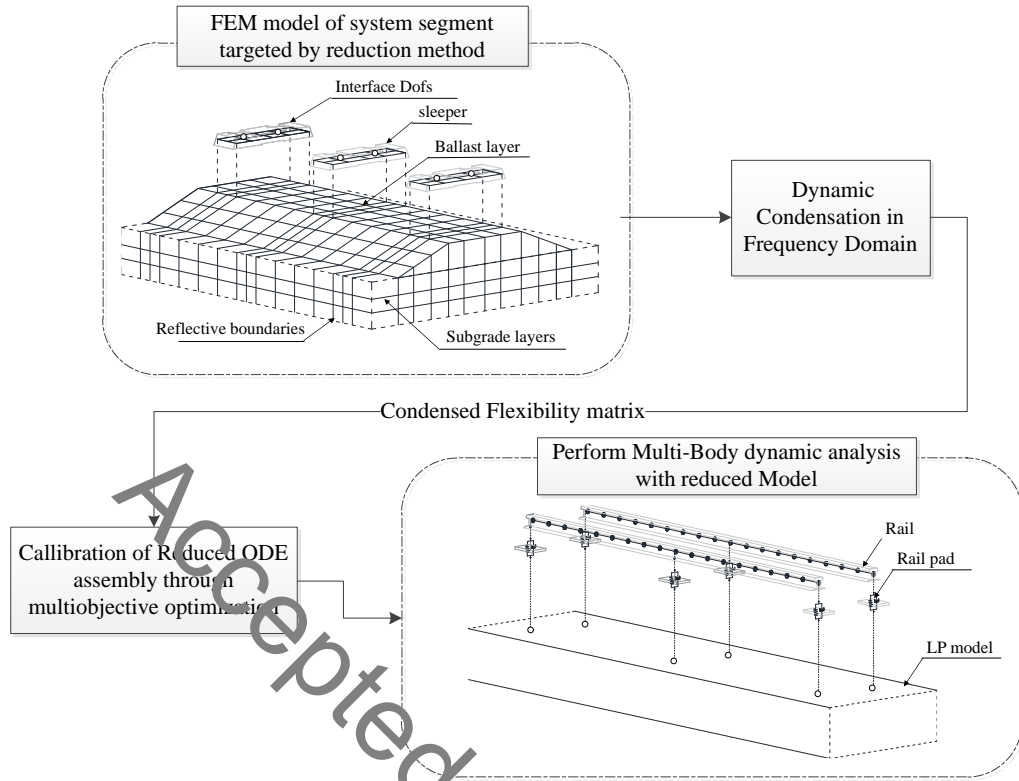


Figure 1. Flowchart of proposed methodology

2.2 Overall system formulation and partition

The mathematical representation of the track– foundation – semi-infinite soil domain system can be illustrated in the classic ordinary differential equation (ODE) formulation after the appropriate geometrical discretization of the original partial differential equation system through the finite element method.

$$\mathbf{M} \cdot \ddot{\mathbf{u}} + \mathbf{C} \cdot \dot{\mathbf{u}} + \mathbf{f}(\mathbf{u}) = \mathbf{F} \quad (1)$$

The variables \mathbf{M} and \mathbf{C} denote the mass and damping coefficient matrices of the overall vehicle-track-soil system, $\mathbf{f}(\mathbf{u})$ denotes the force to displacement relation vector while \mathbf{F} is the external loading vector applied to the respective degrees of freedom (DOFs).

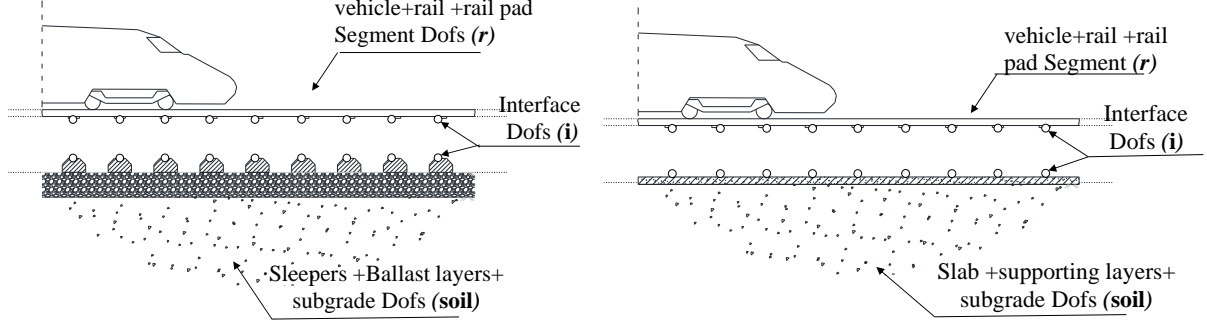


Figure 2. Illustration of the region partition for a) the ballasted track and b) ballastless track systems

The overall system can be partitioned into individual segments by selecting regions where order reduction criteria are fulfilled. The partition methodology for two conceptually different types of track systems, the ballasted track and the slab track system, are illustrated in figures 2a and 2b respectively. In the ballasted track scenario, the sleepers along with the ballast, subballast and subsoil layers are included in the system segment targeted by the order reduction approach. For the slab track scenario, a similar strategy is followed where the slab supporting layers and subsoil layers are included in the reduced segment of the system. The overall system's individual partitions are notated as r , $soil$ and i corresponding to the vehicle-rail-rail pad segment, the foundation-subsoil segment and the interface segment DOFs respectively. The vehicle-rail-rail pad segment is not affected by the model order reduction process and can be simulated by any multi-body train-track interaction method available in the literature. For example, in the experimental case study of section 5, the car body, bogies, and wheel-sets are modelled as mass blocks, the suspension systems as springs and dampers while interaction between the vehicle and rail is simulated in accordance with [31]. Through the aforementioned notation, the dynamic system of equation (1) is expanded according to the selected segmentation.

$$\mathbf{u} = \begin{bmatrix} \mathbf{u}_r \\ \mathbf{u}_i \\ \mathbf{u}_{soil} \end{bmatrix}, \quad \mathbf{M} = \begin{bmatrix} \mathbf{M}_{r,r} & \mathbf{0} & \mathbf{0} \\ \mathbf{0} & \mathbf{M}_{i,i}^r + \mathbf{M}_{i,i}^{soil} & \mathbf{0} \\ \mathbf{0} & \mathbf{0} & \mathbf{M}_{soil,soil} \end{bmatrix}, \quad \mathbf{C} = \begin{bmatrix} \mathbf{C}_{r,r} & \mathbf{C}_{r,i} & \mathbf{0} \\ \mathbf{C}_{i,r} & \mathbf{C}_{i,i}^r + \mathbf{C}_{i,i}^{soil} & \mathbf{C}_{i,soil} \\ \mathbf{0} & \mathbf{C}_{soil,i} & \mathbf{C}_{soil,soil} \end{bmatrix}$$

$$\mathbf{f}(\mathbf{u}) = \begin{bmatrix} \mathbf{f}_r(\mathbf{u}_r, \mathbf{u}_i) \\ \mathbf{f}_i(\mathbf{u}_r, \mathbf{u}_i) \\ \mathbf{0} \end{bmatrix} + \begin{bmatrix} \mathbf{0} & \mathbf{0} & \mathbf{0} \\ \mathbf{0} & \mathbf{K}_{i,i}^{soil} & \mathbf{K}_{i,soil} \\ \mathbf{0} & \mathbf{K}_{soil,i} & \mathbf{K}_{soil,soil} \end{bmatrix} \cdot \begin{bmatrix} \mathbf{u}_r \\ \mathbf{u}_i \\ \mathbf{u}_{soil} \end{bmatrix}, \quad \mathbf{F} = \begin{bmatrix} \mathbf{F}_r \\ \mathbf{F}_i \\ \mathbf{0} \end{bmatrix} \quad (2)$$

In equation (2) subscripts denote the segment where the DOF is located, while the superscripts used only on the interface DOF terms denote the segment from which the contributing stiffness, mass or damping is originating.

2.3 Order reduction in the frequency domain

A basic requirement for the proposed methodology is to represent the wave propagation, refraction and reflection phenomena within a ballast-subsoil system (or slab-subsoil system for the ballastless track case) in a compact yet accurate manner. This is accomplished through the use of the dynamic flexibility matrix in the frequency domain capable of mapping the displacement of the ballast-subsoil domain at any given location $u_i(t)$ with a loading excitation $f_k(t)$ applied somewhere in the medium, taking into account all dynamic phenomena contributing in the displacement response as illustrated in [figure 3](#). The transfer function $H_{k,l}$ for a specific load location k and displacement response location l is illustrated in the following equation.

$$F_k(\omega) = H_{k,l}(\omega) \cdot u_l(\omega) \quad (3)$$

$$\text{Where } F_k(\omega) = \int_{-\infty}^{+\infty} f_k(t) \cdot e^{-2\pi i \cdot \xi \cdot t} dt \text{ and } U_l(\omega) = \int_{-\infty}^{+\infty} u_l(t) \cdot e^{-2\pi i \cdot \xi \cdot t} dt$$

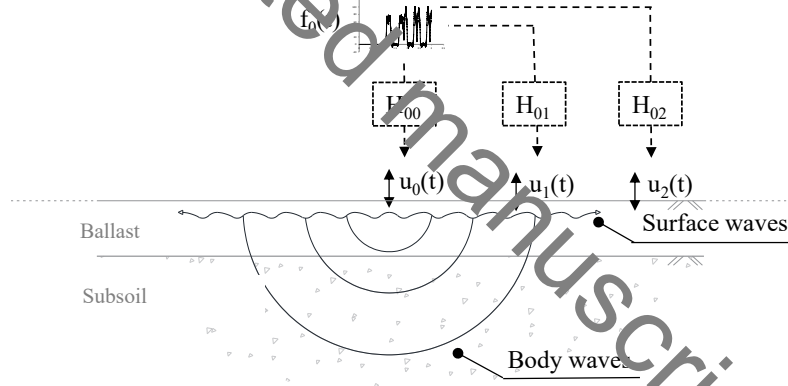


Figure 3. Transfer functions representation in the subsoil-ballast medium

The aforementioned formulation is utilized in the vehicle – track-soil system reduction through the condensation of the equations corresponding to the soil subsoil segment of the system. Since direct condensation is not applicable for the differential equation system, reformulation of the system is essential. The matrix system of [equation \(3\)](#) is initially expanded, while the equation terms of the foundation-subsoil segment are reformed in the frequency domain through the use of the Fourier transformation.

$$\mathbf{M}_{r,r} \ddot{\mathbf{u}}_r + \mathbf{C}_{r,r} \dot{\mathbf{u}}_r + \mathbf{C}_{r,i} \dot{\mathbf{u}}_i + \mathbf{f}_r(\mathbf{u}_r, \mathbf{u}_i) = \mathbf{0} \quad (4)$$

$$\mathbf{M}_{i,i}^r \ddot{\mathbf{u}}_i + \mathbf{C}_{i,i}^r \dot{\mathbf{u}}_i + \mathbf{f}_i(\mathbf{u}_r, \mathbf{u}_i) + \mathbf{C}_{i,r} \dot{\mathbf{u}}_r + \mathcal{F}^{-1}(\mathcal{F}(\mathbf{M}_{i,i}^{soil} \ddot{\mathbf{u}}_i + \mathbf{C}_{i,i}^{soil} \dot{\mathbf{u}}_i + \mathbf{K}_{i,i}^{soil} \mathbf{u}_i + \mathbf{C}_{i,soil} \dot{\mathbf{u}}_{soil} + \mathbf{K}_{i,soil} \mathbf{u}_{soil})) = \mathbf{0} \quad (5)$$

$$\mathcal{F}(\mathbf{M}_{soil,soil}\ddot{\mathbf{u}}_{soil} + \mathbf{C}_{soil,i}\dot{\mathbf{u}}_i + \mathbf{C}_{soil,soil}\dot{\mathbf{u}}_{soil} + \mathbf{K}_{soil,i}\mathbf{u}_i + \mathbf{K}_{soil,soil}\mathbf{u}_{soil}) = 0 \quad (6)$$

The notations \mathcal{F} and \mathcal{F}^{-1} denote the Fourier and the inverse Fourier transformation respectively. Through the use of the dynamic stiffness notation $\mathbf{S}_{ij} = -\mathbf{M}_{ij}\omega^2 + \mathbf{C}_{ij}\omega + \mathbf{K}_{ij}$ equations (5) and (6) take the following form.

$$\mathbf{M}_{i,i}^r\ddot{\mathbf{u}}_i + \mathbf{C}_{i,i}^r\dot{\mathbf{u}}_i + \mathbf{C}_{i,r}\dot{\mathbf{u}}_r + \mathbf{f}_i(\mathbf{u}_r, \mathbf{u}_i) + \mathcal{F}^{-1}(\mathbf{S}_{i,i}^{soil}\mathbf{U}_i + \mathbf{S}_{i,soil}\mathbf{U}_{soil}) = \mathbf{0} \quad (7)$$

$$\mathbf{S}_{soil,soil}\mathbf{U}_{soil} + \mathbf{S}_{soil,i}\mathbf{U}_i = \mathbf{0} \quad (8)$$

The Fourier transformation of a displacement vector \mathbf{u} is denoted with the capital notation \mathbf{U} while the convolution operator is symbolized with the notation “*”. The dynamic system of equation (8) can now be significantly reduced in size through the elimination of the displacement vector \mathbf{U}_{soil} .

$$\mathbf{u} = \begin{bmatrix} \mathbf{u}_r \\ \mathbf{u}_i \end{bmatrix}, \quad \mathbf{M} = \begin{bmatrix} \mathbf{M}_r & \mathbf{0} \\ \mathbf{0} & \mathbf{M}_{i,i} \end{bmatrix}, \quad \mathbf{C} = \begin{bmatrix} \mathbf{C}_{r,r} & \mathbf{C}_{r,i} \\ \mathbf{C}_{i,r} & \mathbf{C}_{i,i} \end{bmatrix}, \quad \mathbf{F} = \begin{bmatrix} \mathbf{F}_r \\ \mathbf{F}_i \end{bmatrix}$$

$$\mathbf{f}(\mathbf{u}) = \begin{bmatrix} \mathbf{f}_r(\mathbf{u}_r, \mathbf{u}_i) \\ \mathbf{f}_i(\mathbf{u}_r, \mathbf{u}_i) \end{bmatrix} + \begin{bmatrix} \mathbf{0} \\ \mathcal{F}^{-1}(\mathbf{H}(\omega)^{-1}) * \mathbf{u}_i \end{bmatrix}$$

Where $\mathbf{H}(\omega) = (\mathbf{S}_{i,i}^{soil} - \mathbf{S}_{i,soil} \cdot \mathbf{S}_{soil,soil}^{-1} \cdot \mathbf{S}_{soil,i})^{-1}$ (9)

The variable $\mathbf{H}(\omega)$ is the N by N dynamic flexibility matrix of the foundation-subsoil segment (reduced segment) and N is the number of DOFs located at the interface region between the reduced segment and the remaining dynamic system as described in the previous section. Due to the specific morphology of the track system it is more convenient to sort the interface DOFs in M number of interface groups corresponding to each rail to slab connection interface or sleeper to rail interface depending on the track type in question. The dynamic flexibility matrix formulated in accordance with the sorted interface groups is illustrated in the following equation, where C corresponds to a selected interface region as the center of the system, while i,L and i,R correspond to the i consecutive interface group on the left and right respectively.

$$\mathbf{H}(\omega) = \begin{bmatrix} \mathbf{H}_{C,C}(\omega) & \mathbf{H}_{C,1L}(\omega) & \mathbf{H}_{C,1R}(\omega) & \cdots \\ \mathbf{H}_{C,1L}(\omega) & \mathbf{H}_{1L,1L}(\omega) & \mathbf{H}_{1R,1L}(\omega) & \\ \mathbf{H}_{C,1R}(\omega) & \mathbf{H}_{1L,1R}(\omega) & \mathbf{H}_{1R,1R}(\omega) & \\ \vdots & & & \ddots \end{bmatrix} \quad (10)$$

The authors exploit a fundamental property of the longitudinally periodic isolated soil-ballast-sleeper system as presented in [8]. For a selected sleeper its direct receptance and coupling to its neighbouring sleepers is identical to any other sleeper along the track. The aforementioned property is implemented in the reduced model flexibility matrix targeting the soil-ballast-sleeper. For the scenario where the transverse direction is neglected, each submatrix corresponds to a single vertical DOF flexibility function ($\mathbf{H}_{ij}(\omega) = H_{ij}(\omega)$).

$$\mathbf{H}_{C,C}(\omega) = \mathbf{H}_{iL,iL}(\omega) = \mathbf{H}_{iR,iR}(\omega) \quad (11)$$

Where $i \in [1, +\infty)$

$$\mathbf{H}_{iL,iL}(\omega) = \mathbf{H}_{kL,kL}(\omega) = \mathbf{H}_{C,qL}(\omega) = \mathbf{H}_{kR,kR}(\omega) = \mathbf{H}_{C,qR}(\omega) \quad (12)$$

Where $i-j = \kappa - l = q$ and $i, j, k, l, q \in [1, +\infty)$

Finally, a finite number of coupling flexibility matrices is taken into account, as the influence between two interface groups with significant distance between them is expected to be negligible and thus have minor impact on the behavior of the overall dynamic system.

3. SYSTEM RECONSTRUCTION IN THE TIME DOMAIN

Upon the completion of the reduction procedure it is essential to recombine the reduced segment with the remaining unaltered system. The remaining vehicle-rail-rail pad segment is formulated in the time domain as illustrated in section 2.1. As a result, the reduced soil-track segment is reconstructed to a compatible version in the time domain, through a multiobjective optimization procedure presented in the following section.

3.1 Selection of the lumped parameter assembly

A predefined ordinary differential equation system, indicated as an infinite lumped parameter (LP) assembly throughout this study, is selected as an appropriate translation of the reduced segment in the time domain in accordance with the longitudinally repeated morphology of the segment. The predefined LP assembly selected for the proposed methodology is illustrated in figure

4.

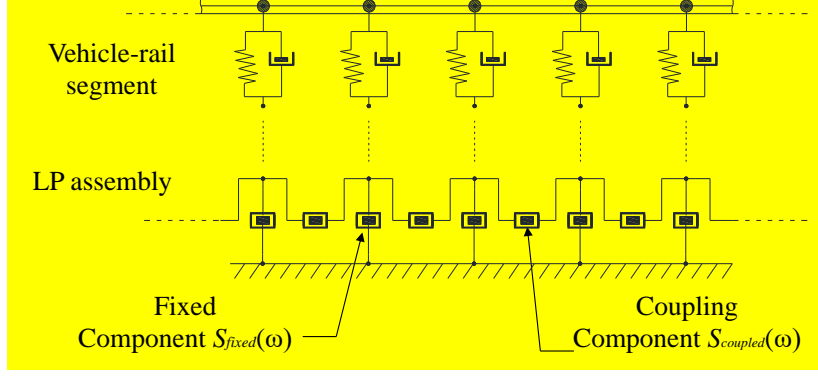


Figure 4. Single coupled lumped parameter model assembly

The assembly is defined by a recursive pattern of LP models indicated as $LP_{coupling}$ and LP_{fixed} respectively. Each LP model is composed of a group of springs, dashpots and mass components. In contrast to the fixed LP models, the coupling LP models dynamically connect two individual DOFs. The relationship between diagonal and off-diagonal dynamic stiffness terms can be derived upon selection of the components comprising the LP model in question.

As previously indicated, the calibration of the LP assembly targets the dynamic flexibility matrix derived from the reduction procedure of the foundation subsoil segment. As a result, it is essential to derive the frequency domain flexibility matrix of the LP assembly in a similar parametric form prior to the formulation of the optimization procedure. In more detail, the isolated LP assembly system in the frequency domain and under the loading conditions of a dynamic excitation P_{ext} at a location c of the infinite assembly takes the following form:

$$(S_{fixed} + 2 \cdot S_{coupled}) \cdot U_c + S_{coupled}^{off} \cdot U_{1,L} + S_{coupled}^{off} \cdot U_{1,R} = P_{ext} \quad (13)$$

$$(S_{fixed} + 2 \cdot S_{coupled}) \cdot U_{1,L} + S_{coupled}^{off} \cdot U_c + S_{coupled}^{off} \cdot U_{2,L} = 0 \quad (14)$$

$$(S_{fixed} + 2 \cdot S_{coupled}) \cdot U_{n,L} + S_{coupled}^{off} \cdot U_{n-1,L} + S_{coupled}^{off} \cdot U_{n+1,L} = 0 \quad (15)$$

$$\text{due to symmetry: } U_{n,L} = U_{n,R} \quad \text{infinite boundaries: } n \in [2, +\infty) \quad (16)$$

The parameter U_i corresponds to the Fourier transformation of the displacement time history u_i at the location i and n is the sequence number of the interface group. S_{fixed} corresponds to the dynamic stiffness of the fixed component and $S_{coupled}$ and $S_{coupled}^{off}$ are the direct and cross terms of the dynamic stiffness matrix of the coupling component. The displacement Fourier transformation ratio U_{n+1}/U_n , between successive interface groups can be depicted in a recursive manner as illustrated in the following equation.

$$\frac{U_{n+1}}{U_n} = \frac{S_{coupled}^{off}}{S_{fixed} + 2 \cdot S_{coupled}^{diag} - \frac{S_{coupled}^{off \ 2}}{S_{fixed} + 2 \cdot S_{coupled}^{diag} - \frac{S_{coupled}^{off}}{\ddots}}} \quad (17)$$

By direct substitution of equation (17) back into equations (13) and (14) and isolation of the displacement to excitation Fourier transformation ratio, the flexibility dynamic matrix of the LP assembly takes the following form.

$$H_{C,C} = \frac{R_\infty}{R_\infty^2 - S_{coupled}^{off \ 2}}, \quad H_{C,jL} = H_{C,jR} = \left(-\frac{S_{coupled}^{off}}{R_\infty} \right)^j \cdot H_{C,C}$$

Where
$$R_\infty = \frac{S_{fixed} + 2 \cdot S_{coupled}^{diag} - \frac{S_{coupled}^{off \ 2}}{S_{fixed} + 2 \cdot S_{coupled}^{diag} - \frac{S_{coupled}^{off \ 2}}{S_{fixed} + 2 \cdot S_{coupled}^{diag} - \frac{S_{coupled}^{off}}{\ddots}}}}{S_{fixed} + 2 \cdot S_{coupled}^{diag} - \frac{S_{coupled}^{off \ 2}}{S_{fixed} + 2 \cdot S_{coupled}^{diag} - \frac{S_{coupled}^{off}}{\ddots}}} \quad (18)$$

The term R_∞ demonstrates a recursive sequence pattern as illustrated in equation (18). As the R_∞ recursive sequence is increasing and bounded above, it is possible to calculate the value of the sequence for the infinite boundary conditions ($n \rightarrow \infty$) by applying the appropriate limits and solving for the unknown R_∞ .

$$a_{n+1} = S_{fixed} + 2 \cdot S_{coupled}^{diag} - \frac{S_{coupled}^{off \ 2}}{a_n} \quad (19)$$

$$R_\infty = \lim_{n \rightarrow \infty} a_{n+1} = \lim_{n \rightarrow \infty} a_n = \sqrt{\frac{(S_{fixed} + 2 \cdot S_{coupled}^{diag})^2}{4} - S_{coupled}^{off \ 2} + \frac{S_{fixed} + 2 \cdot S_{coupled}^{diag}}{2}} \quad (20)$$

The remaining terms of the dynamic flexibility matrix of the LP assembly can be derived from equations 11 and 12, as the LP assembly is periodic.

The required degree of coupling between successive interface groups is determined directly from the targeted flexibility matrix generated from the FEM model, thus no additional restrictions are essential other than the optimization procedure presented in the following sections. Furthermore, there are no limitations in the degree of coupling as both significant and insignificant coupling can be captured by the LP assembly. This is better illustrated by the correlation between the gradual decrease of the vertical displacement, and the Euclidian norm of the fading out ratio $S_{coupled}(\omega)/R_{\infty}(\omega)$.

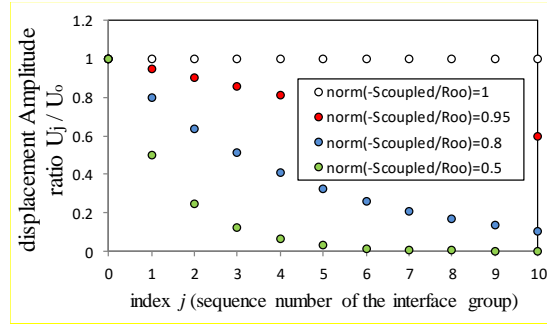


Figure 5. displacement amplitude ratio to sequence number of interface group

Figure 5 illustrates the amplitude of vertical displacement of eleven consecutive sleepers for a harmonic load with frequency ω assigned on the $j=0$ sleeper. In the figure different values of the fading out ratio are included corresponding to different degree of coupling between the interface regions.

3.2 Selection of lumped parameter components

The infinite LP assembly presented in the previous paragraph consists of individual LP models taking the role of directly fixed and coupling dynamic springs. A predefined design of the LP models with constrained parameters is utilized in the current study, retaining the stability and passivity properties of the target dynamic system as suggested in [21].

For the role of the fixed dynamic spring, the configuration of the LP model is illustrated in figure 6. The dynamic stiffness S_{fixed} of the fixed LP model is derived from the direct solution of the model's equations of motion transformed in the frequency domain in accordance with the component notation depicted in figure 6.

$$S_{fixed} = K - M \cdot \omega^2 + C \cdot \omega i + \sum_{i=1}^N \left(\frac{(k_i + c_{i,up} \cdot \omega i)(-m_i \cdot \omega^2 + c_{i,down} \cdot \omega i)}{k_i + c_{i,up} \cdot \omega i - m_i \cdot \omega^2 + c_{i,down} \cdot \omega i} \right) \quad (21)$$

For the role of the coupling dynamic spring, the selected LP model is illustrated in figure 7a. For the simulation of the coupled behavior between different interface groups, conventional dashpots and springs provide limited emulating capabilities. This limitation is attributed to the nature of coupling terms of conventional springs and dashpots applying relationships in the same direction. However, it is possible to cope with this issue by also including modified springs and dashpots with positive coupling terms. This approach will retain the stability of the overall dynamic system as the damping and stiffness matrices remain positive definite. However, for reasons of

applicability in conventional FEM software, a simplified spring and dashpot coupling system is also included as an alternative option.

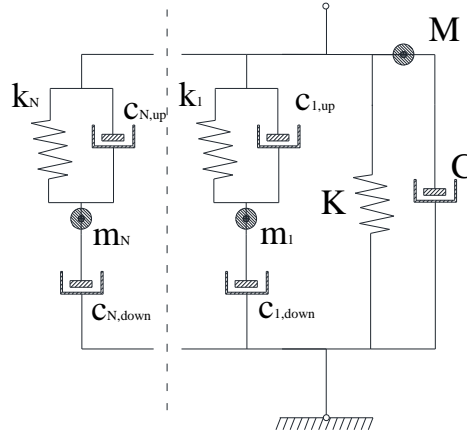


Figure 6. Fixed lumped parameter model

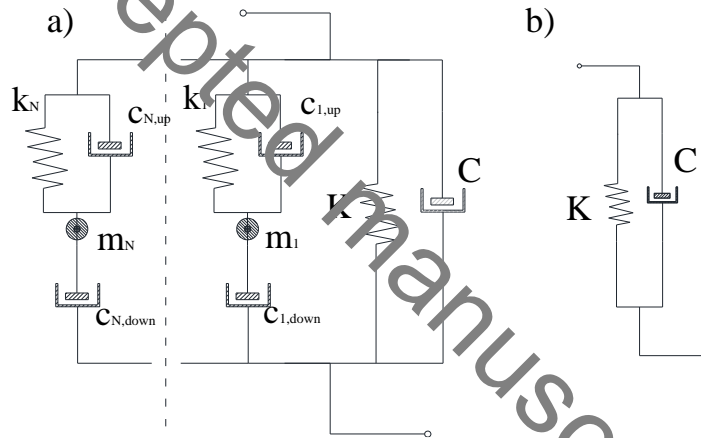


Figure 7. Coupling lumped parameter model a) complete version b) simplified version

The dynamic stiffness functions $S_{coupled}^{diag}$ and $S_{coupled}^{off}$ of the complete coupling LP model (briefly referred to as Cpl. Com.) are derived from the direct solution of the model's equations of motion transformed in the frequency domain in accordance with the component notation depicted in figure 7a.

$$S_{coupled}^{diag} = 2 \cdot K + 2 \cdot C \cdot \omega i + \sum_{i=1}^N \left(k_i + |c_i| \cdot \omega i - \frac{k_i^2 + (c_i \cdot \omega i)^2}{k_i + |c_i| \cdot \omega i - m_i \cdot \omega^2} \right) \quad (22)$$

$$S_{coupled}^{diag} = -K - C \cdot \omega i + \sum_{i=1}^N \left(\frac{k_i \cdot c_i}{k_i + |c_i| \cdot \omega i - m_i \cdot \omega^2} \right) \quad (23)$$

3.3 Assembly calibration through multi-objective optimization

The infinite LP assembly presented in the previous section is composed of numerous dashpot, spring and mass subcomponents. The subcomponent parameters are calibrated by targeting the extracted dynamic flexibility matrix derived in section 2. The calibration procedure can take the following multi-objective optimization form.

$$\begin{aligned} \min_{\mathbf{x}} \quad & (f_{C,C}(\mathbf{x}), f_{C,1L}(\mathbf{x}), \dots, f_{C,mL}(\mathbf{x})) \\ \text{subject to} \quad & \mathbf{x} \geq l_b \\ f_k = \sum_{i=1}^N & [\operatorname{Re}(H_k^{tar}(\omega_i)) - \operatorname{Re}(H_k^{LP}(\omega_i, \mathbf{x}))]^2 + \sum_{i=1}^N [\operatorname{Im}(H_k^{tar}(\omega_i)) - \operatorname{Im}(H_k^{LP}(\omega_i, \mathbf{x}))]^2 \end{aligned} \quad (24)$$

Each objective function f_k corresponds to the efficiency of the LP model with subcomponent parameters \mathbf{x} in emulating the dynamic flexibility function H_k . Scalarization of f_k is accomplished through the weighted-sum method [32], following an a priori preference of unity weights for the squared difference between the targeted H_k^{tar} and LP assembly flexibility function H_k^{LP} . Index m corresponds to the maximum distance between interface regions where coupling is non-negligible. Finally the values of the lower boundary constraint l_b are equal to $-\infty$ for the upper dashpot subcomponents of the coupling LP model c_{up} and equal to 0 for the remaining subcomponents.

The multiobjective optimization problem illustrated in equation (24) can be further decomposed into two single objective optimization problems by focusing on the direct flexibility and 1st cross flexibility functions $H_{C,C}$ and $H_{C,1L}$.

$$\begin{aligned} \min_{\mathbf{x}} \quad & S_{\text{cross}}^{\text{LP}} - \frac{1}{2} \cdot \left(\frac{1}{H_{C,C} + H_{C,1L}} - \frac{1}{H_{C,C} - H_{C,1L}} \right) \\ \text{subject to} \quad & \mathbf{x} \geq l_b \end{aligned} \quad (25)$$

$$\begin{aligned} \min_{\mathbf{x}} \quad & \left[S_{\text{fixed}}^{\text{LP}} - \frac{\left(\sqrt{S_{\text{cross,off}}^{\text{LP}}{}^2 + \frac{1}{4 \cdot (H_{C,C}^{tar})^2} + \frac{1}{2 \cdot H_{C,C}^{tar}}} \right)^2 + (S_{\text{cross,off}}^{\text{LP}})^2}{\sqrt{S_{\text{cross,off}}^{\text{LP}}{}^2 + \frac{1}{4 \cdot (H_{C,C}^{tar})^2} + \frac{1}{2 \cdot H_{C,C}^{tar}}}} - 2 \cdot S_{\text{cross,diag}}^{\text{LP}} \right] \\ \text{subject to} \quad & \mathbf{x} \geq l_b \end{aligned} \quad (26)$$

The decomposed optimization problem provides solutions that optimally capture the direct and 1st cross flexibility functions, while the remaining flexibility functions $f_{C,2L}$ to $f_{C,mL}$ are simulated in accordance with the fading out ratio of the LP assembly (equation 18). The efficiency of the decomposed optimization problem is assessed during the verification of the proposed methodology in the following section.

The optimization problems of equation (25) and equation (26) are solved through the combined efforts of a deterministic search method operating on a local level and a general plan operating on a global level. The search method selected for the local level is the interior point trust region approach proposed by Coleman and Li [33]. The global level general plan is achieved through the multiple execution of the interior point trust region method, initiated from different stochastically generated variable combinations \mathbf{x}_i inside a prediction region. The termination criteria for the proposed optimization scheme consists of an iterative evaluation of the objective function value for the normalized static stiffness of the LP model, along with a maximum boundary on the number of the overall sampling points \mathbf{x}_i .

The proposed method introduces a few limitations to the analysis of a soil-track interacting system, namely (1) the soil is modelled with a viscous elastic constitutive law, an assumption not always valid for high speed trains traveling on soft soil profiles and (2) the track is periodic on the longitudinal direction.

4. NUMERICAL VERIFICATION OF PROPOSED METHODOLOGY

As presented in the previous paragraphs, the proposed procedure can provide a computationally viable alternative for the simulation of vehicle-track dynamic systems. The main goal of the proposed procedure is to accurately capture the complex wave propagation phenomena taking place within the subgrade medium. To this end, a validation of the proposed procedure is essential, thus a numerical case study is presented in the following paragraph. More specifically, a ballasted track set on a multilayer cohesionless soil medium is selected as the case study reference system for which a detailed 3D FEM model is constructed. The 3D finite element model has been verified in a preliminary stage for a single isolated sleeper on a homogeneous half-space. This is accomplished initially with pulse excitations monitoring the amplitude of the waves reflected on the artificial boundaries and secondly with the closed form solution of shallow foundation impedance functions [34]. The constructed FEM model includes a 40m x 60m truncated region of the semi-infinite soil domain, where frequency domain absorbing boundaries are introduced at the sides and bottom of the model in accordance with [35,36]. Both the soil and ballast are simulated with hexahedral finite

elements with sizes from 0.2m to 2m. The construction of the dynamic stiffness matrix of the FEM model is accomplished by direct summation of the Fourier transformation of the truncated FEM system and the frequency domain generated Novak boundaries.

$$\mathbf{S}_{soil,soil} = -\mathbf{M}_{soil,soil}^{FEM} \cdot \omega^2 + \mathbf{C}_{soil,soil}^{FEM} \cdot \omega i + \mathbf{K}_{soil,soil}^{FEM} + \mathbf{S}_{soil,soil}^{Bound,Novak} \quad (27)$$

The reference track is founded on a cohesionless soil profile with parabolic distribution of elastic modulus along the depth as depicted in figure 8 ($E_{z=9m}=48.3\text{Mpa}$, $E_{z=7m}=66.7\text{Mpa}$, $E_{z=5m}=88.4\text{Mpa}$, $E_{z=3m}=106.7\text{Mpa}$ and $E_{z=1m}=122.9\text{Mpa}$) with specific density $\gamma = 1.9 \text{ t/m}^3$ and Poisson ratio $\nu = 0.40$. A single ballast layer is considered with a depth of $z_b = 0.3 \text{ m}$ and with elastic modulus $E_b = 270 \text{ MPa}$, specific density $\gamma = 2 \text{ t/m}^3$ and Poisson ratio $\nu = 0.3$. The rail pads used have a stiffness of $K_r = 100000 \text{ kN/m}$ and the rail moment of inertia is equal to $I = 3038.3 \text{ cm}^4$ for each rail. The distance between two consecutive sleepers is 0.6 m and the sleeper mass has a value of $m = 0.3 \text{ t}$.

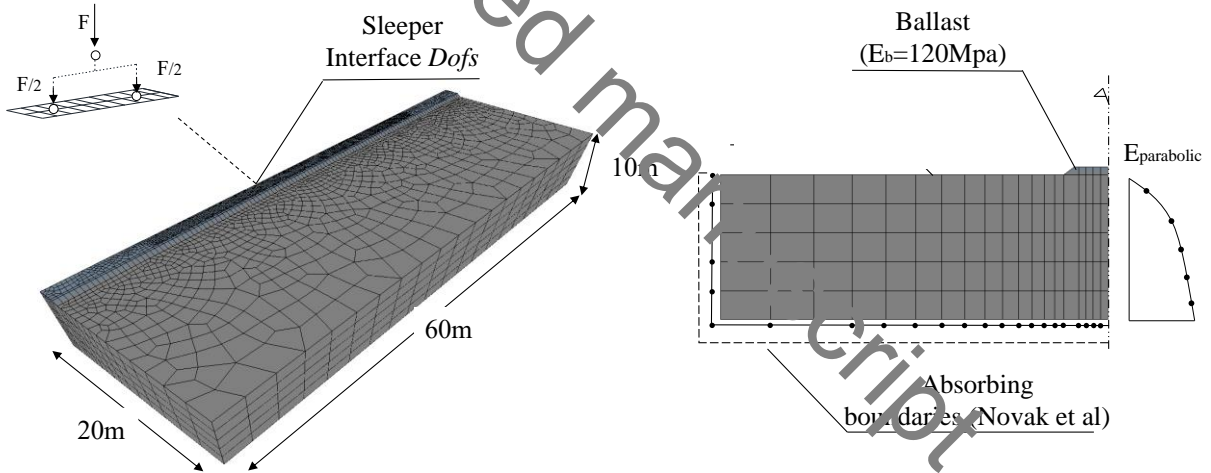


Figure 8. Finite Element model of foundation subsoil segment

The proposed method efficiency and two additional simplified modeling options, namely (1) the popular representation of the subsoil and ballast with Kelvin-Voigt models and (2) a simplified discrete model proposed by Kouroussis [25] with coupling taken into account through an additional Kelvin-Voigt component are evaluated in reference to the detailed 3D FEM model. The parameter values for the four models included in the case study can be found in Appendix A.

4.1 LP model calibration in the frequency domain

The isolated segment's flexibility function $\mathbf{H}(\omega)$ is extracted from the detailed FEM model through the dynamic condensation of the system in the frequency domain as presented in equation (9). The extracted dynamic flexibility functions are used as a target for the calibration of two different LP assemblies, an LP assembly with the complete LP coupling model figure 7a and one with the simplified LP coupling model figure 7b.

The efficiency of the decomposed optimization scheme of equation (25) and equation (26) is assessed for the particular case study through the comparison of the solutions derived from the multi-objective optimization version of equation (24) as illustrated in figure 9. The pareto front for the direct $f_{c,c}$ and first cross $f_{c,IL}$ objective functions is calculated through the use of a multi-objective implementation of the particle swarm optimization (PSO) method [37].

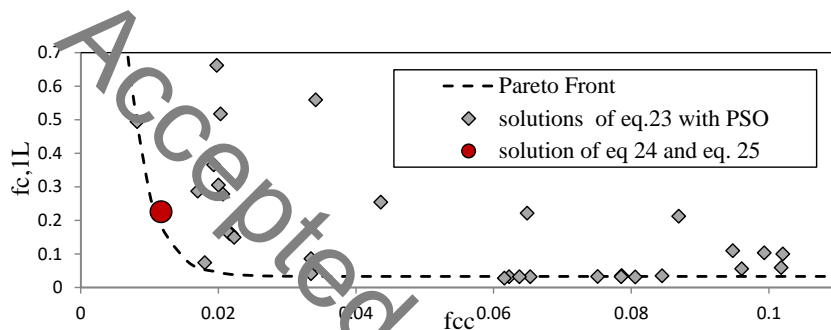


Figure 9. Location of solution in Pareto front

The calibration efficiency of the simplified coupling and complete coupling LP assemblies are illustrated in figure 10 for the direct, 1st and 2nd cross dynamic flexibility functions. As observed in figure 10, the direct dynamic flexibility function $H_{c,c}$ of the targeted dynamic system is accurately captured by both the complete and simplified coupling LP assemblies. On the other hand, the 1st cross dynamic flexibility function $H_{c,IL}$ is not accurately represented by the simplified coupling LP assembly for a frequency higher of 40 Hz. This can be attributed to the fact that the simplified coupling component of figure 7b cannot capture the oscillating behaviour of the targeted cross dynamic flexibility functions indicated in higher frequencies. For the remaining cross flexibility function a small divergence is observed in the 20-40Hz range in the complete coupling LP assembly while a higher divergence in the 20-100Hz range is observed in the simplified coupling LP assembly.

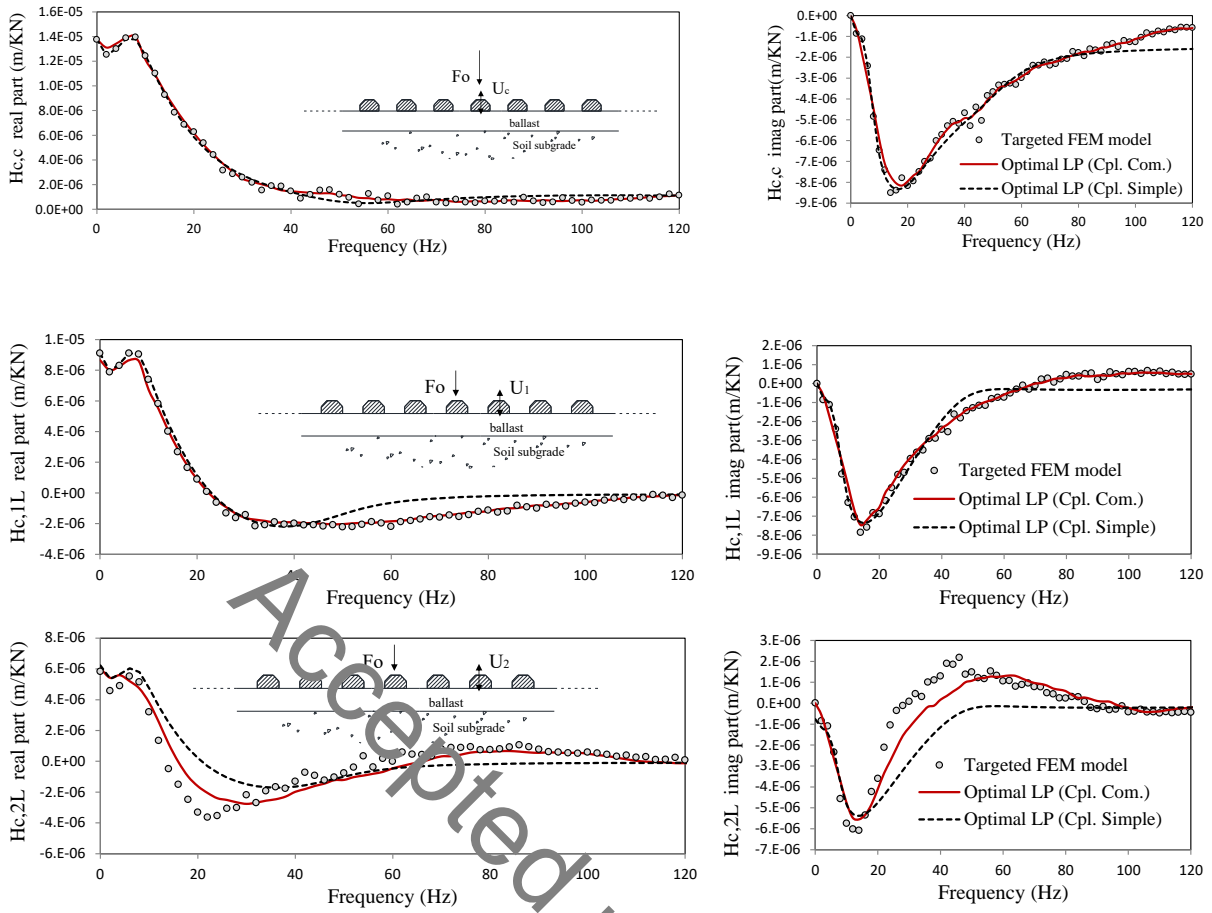


Figure 10. Optimization results of LP assemblies for dynamic flexibility matrix terms

a) $H_{c,c}$ b) $H_{c,1L}$ c) $H_{c,2L}$

The success of the proposed methodology is illustrated in figure 11 by comparing the direct receptance function of the complete track system between the targeted FEM model and the two LP assemblies presented in the previous section.

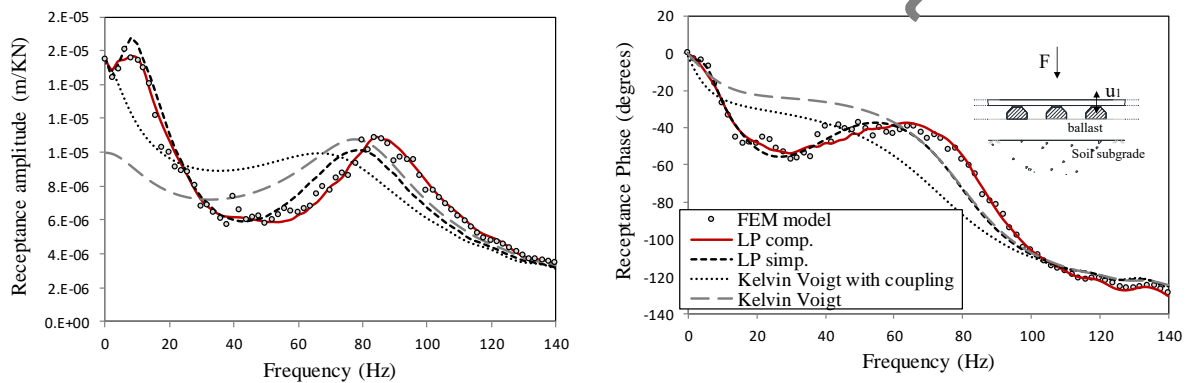


Figure 11. Comparison of receptance amplitude and receptance phase of soil-track system

As observed in [figure 11](#) the rail-railpad system dominates the response of the overall track system for the higher frequency range while the subsoil representation mainly influences the track system behavior in the lower frequency range. The complete coupling LP assembly closely approximates the targeted receptance for the overall frequency range with Mean Absolute Percentage (MAP) error lower than 4%. A higher error is observed in the simplified coupling LP assembly for the frequency range 30-80Hz. On the scenarios of the Kelvin-Voigt and Kouroussis et al simplified methodologies it can be observed that for the multilayer soil profile the dynamic characteristics of the subgrade medium are not accurately captured.

4.2 Time domain numerical verification

The final part of the numerical verification case study is focused on the model's competence in capturing the track response for trains approaching the critical velocity of the subsoil medium. It is important to state that the phenomenon of deformation amplification in the railway track due to a train moving near the critical velocity of the medium is now also influenced by the contribution of body waves reflected by the lower stiffer layers of the selected multilayer soil profile. The response of the railway track is calculated for the detailed FEM model under the excitation of a moving load of $W_z=200$ kN running at three individual constant velocities of $v_1=68$ km/h, $v_2=347$ km/h and $v_3=470$ km/h. The selected velocities correspond to subcritical, near critical and post critical values for the specific multilayered soil-track system. The absolute displacement amplification factor (DAF) on the ground surface for the selected velocities is illustrated in [figure 12](#), as generated by the FEM model.

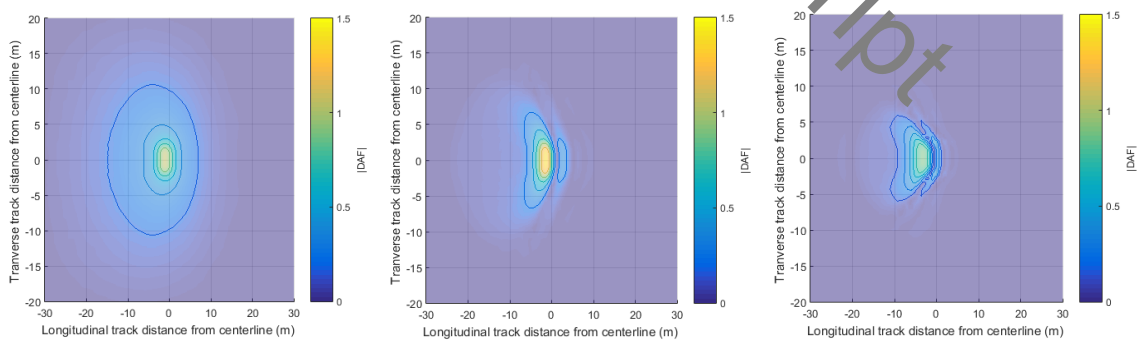


Figure 12. Vertical displacement amplification on ground surface for a) $v_1=86$ km/h b) $v_2=347$ km/h c) $v_3=470$ km/h

The rail deflection response for the proposed LP methods along with the previously selected simplified methodologies are compared with the 3D FEM model rail deflection response as illustrated in [figure 13](#).

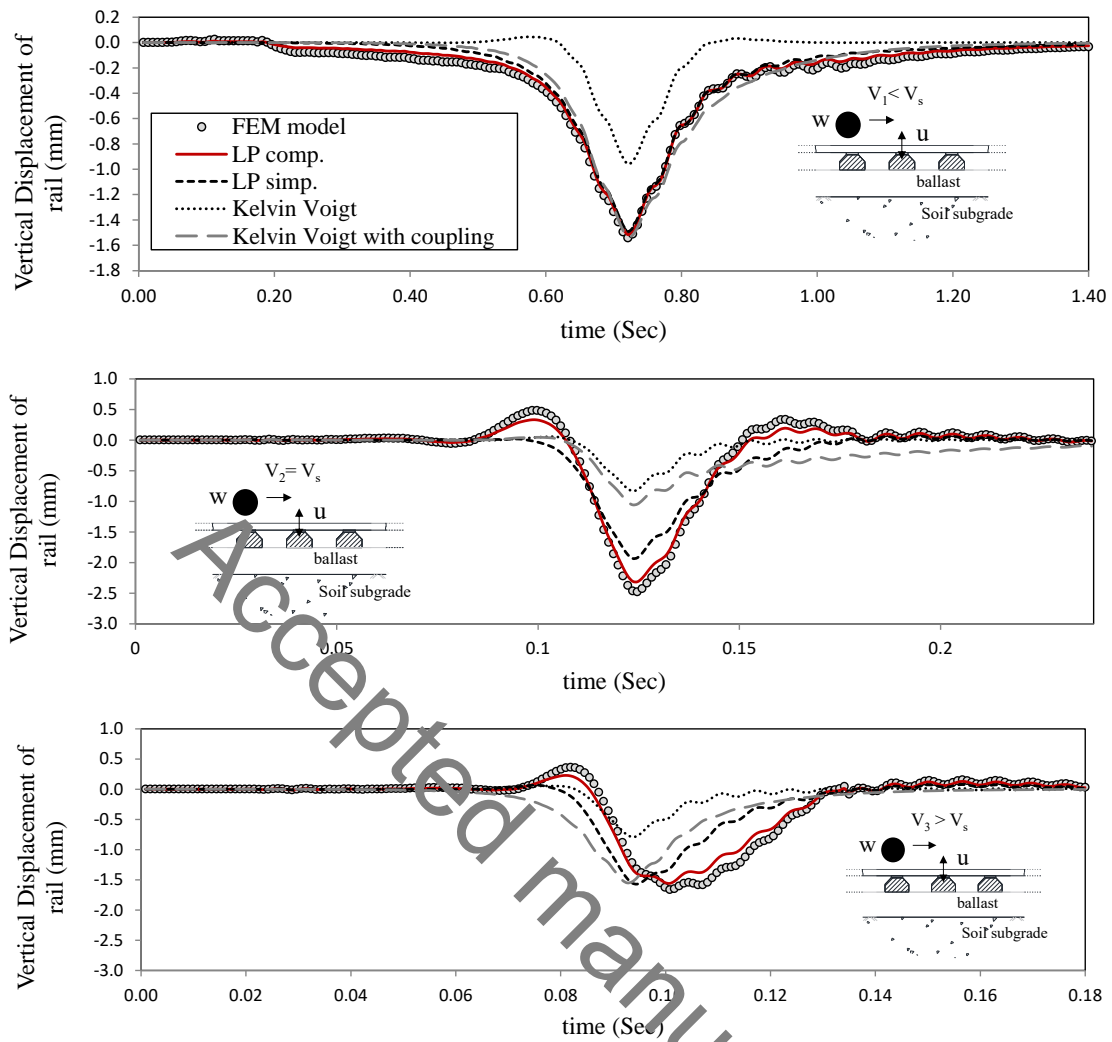


Figure 13. Rail vertical displacement time history for load moving in a) $v_1=86\text{ km/h}$ b) $v_2=347\text{ km/h}$ c) $v_3=470\text{ km/h}$

The results depicted in figure 13 indicate the importance of an accurate representation of the frequency dependent coupling subsoil behavior. As observed with both the Kouroussis et al and the simplified LP methodologies, an approximate representation of the coupling behavior will not necessarily lead to a correct simulation of the wave propagation phenomena within the soft multilayered subsoil medium. This phenomenon is especially highlighted for the near critical speed load velocity ($v=347\text{ km/h}$). As observed in figure 14, the pulse excitations from the moving load applied in the rail-track system indicate a Fourier amplitude concentration in the frequency range of 0-120Hz. The mean absolute percentage error (MAPE) [38] of the track receptance function for the simplified LP approach is mainly concentrated in the 40-120 Hz frequency region. The source of inaccuracy for the specific frequency region is well illustrated in figures 9b and 9c where the 1st and 2nd cross receptances diverge from the targeted extracted behavior. Furthermore, the error

introduced by the non-coupling Kelvin-Voigt method leads to a significant error in the representation of both dynamic and static properties of the soft subsoil system.

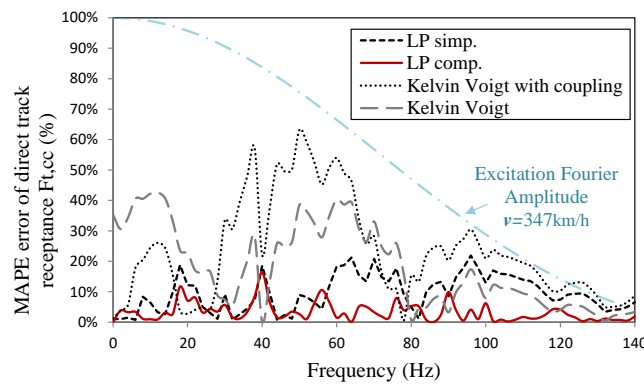


Figure 14. MAPE error of direct track receptance function for the different simulation methods

Finally, the peak vertical track displacement as a function of train speed for a moving load velocity range of 80km/h to 520km/h is illustrated in figure 15. The results here further reinforce the conclusion that the correct representation of the frequency dependent behavior of the direct and cross receptances of the subsoil-track system is a mandatory requirement for the simulation of track systems founded in a multilayered soil medium. In more detail, the error of the direct receptance function of the overall track-soil system by the three simplified methods leads to an inaccurate estimation of the peak vertical displacement. Since the simplified LP method's inefficiency to capture the receptance function is limited in the frequency range of 40-120 Hz, the peak vertical displacement is accurately estimated up to a velocity of 280km/h, while the remaining simplified methods introduce an inaccurate representation along the overall velocity range of importance.

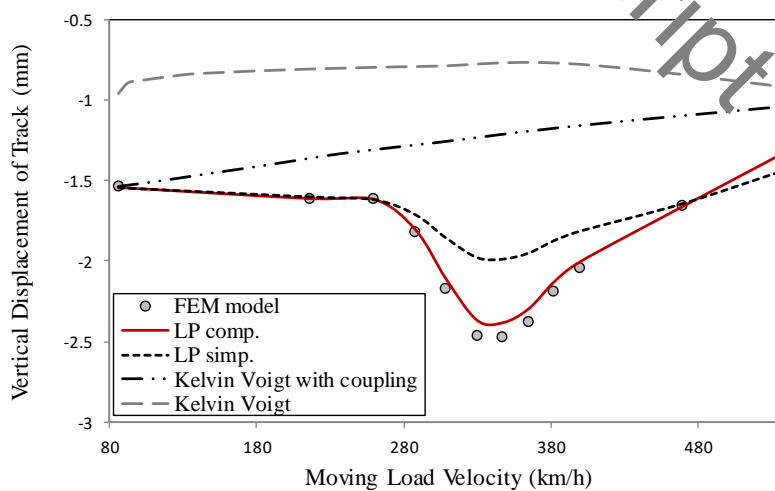


Figure 15. Maximum downward vertical track displacement versus train speed for the selected modeling methods

5. COMPLEMENTARY EXPERIMENTAL VERIFICATION

Finally, the proposed methodology is experimentally verified with rail displacement measurements of a ballastless track excited by the ICE2 high-speed train power car. The power car is attached to a modified wagon with measurement equipment. Data has been extracted from instrumentations of a section of a modern high-speed track in mainland Europe. The top view in **Figure 16b** illustrates locations of several displacement sensors recording the relative displacement between rail foot and top of slab track (blue) and vertical displacement sensors between top of slab track and top of sub grade (green and red). For clarification **Figure 16a** depicts the sensors in the cross-sectional view for an isolated rail of the ballastless track. The available measurements have been extracted using the ICE2 test-train consisting of one power car and one passenger car operating with a constant velocity of 160 km/h. The relative displacement between rail foot (blue sensor) and top of concrete serves as the reference solution for the numerical model.

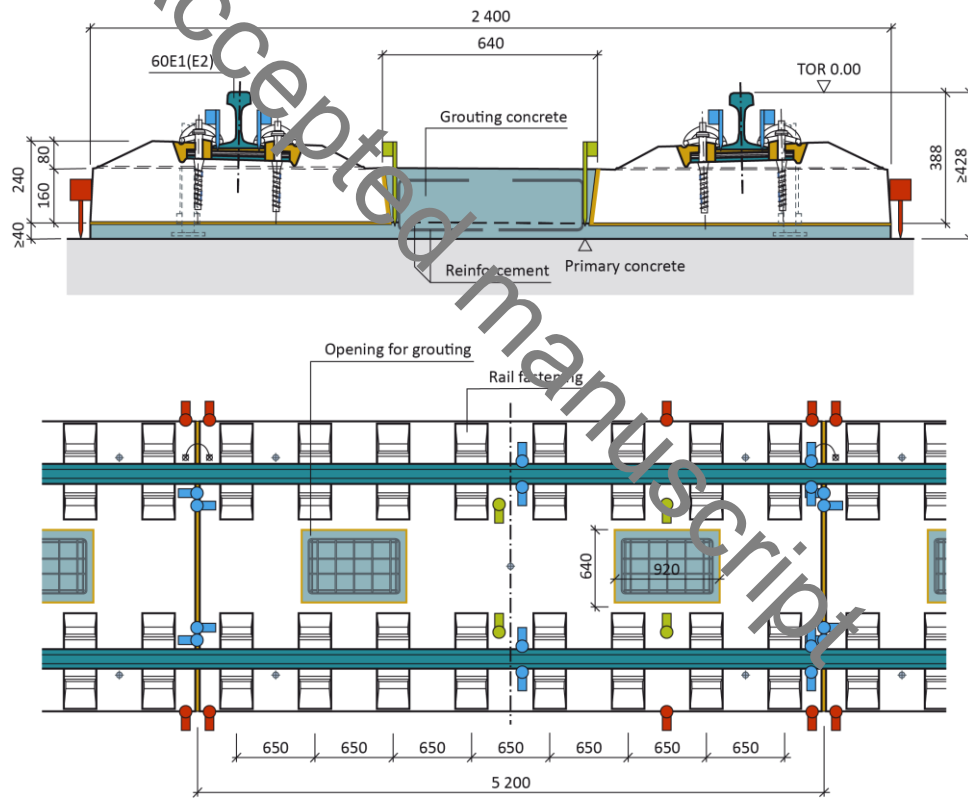


Figure 16.a) Cross section of the monitoring assembly at an isolated rail b) top view of the monitoring assembly

The ballastless track system is simulated by the proposed LP model with coupling terms according to **figure 7.b**. The calibration of the LP model targets a truncated FEM model constructed according to the guidelines presented in the previous section. The rail moment of inertia is equal to $I = 3038.3 \text{ cm}^4$ for each rail, while the support spacing is equal to $s_x = 0.65 \text{ m}$. **The slab properties used in the analysis are those of the equivalent rectangular section slab with young modulus**

$E=29\text{GPa}$, height $h=0.4\text{m}$ and width $w=2.4\text{m}$. Since soil conditions on site are not available, a uniform soil profile with shear wave velocity $v_s = 190 \text{ m/s}$, Poisson ratio $\nu = 0.41$ and density $\rho = 1.8 \text{ t/m}^3$ has been numerically reverse engineered in accordance with plate load test calculations [34] of the strain modulus equal to $E_{v2} = 120 \text{ MPa}$.

The vehicle model, illustrated in figure 17b, is simulated according to the rigid-body dynamics method [31], where the car body, bogies, and wheel-sets are simplified as mass blocks, and the suspension systems as springs and dampers. The component parameters for the ICE2 power car can be found in [39] ($M_C=60.8\text{t}$, $\theta_C=1344\text{tm}^2$, $M_b=5.6\text{t}$, $\theta_b=21.84\text{tm}^2$, $M_w=2\text{t}$, $K_{s1}=9600\text{KN/m}$, $C_{s1}=30 \text{ KN*s /m}^3$, $K_{s2}=3520\text{KN/m}$, $C_{s2}=80 \text{ KN*s /m}^3$).

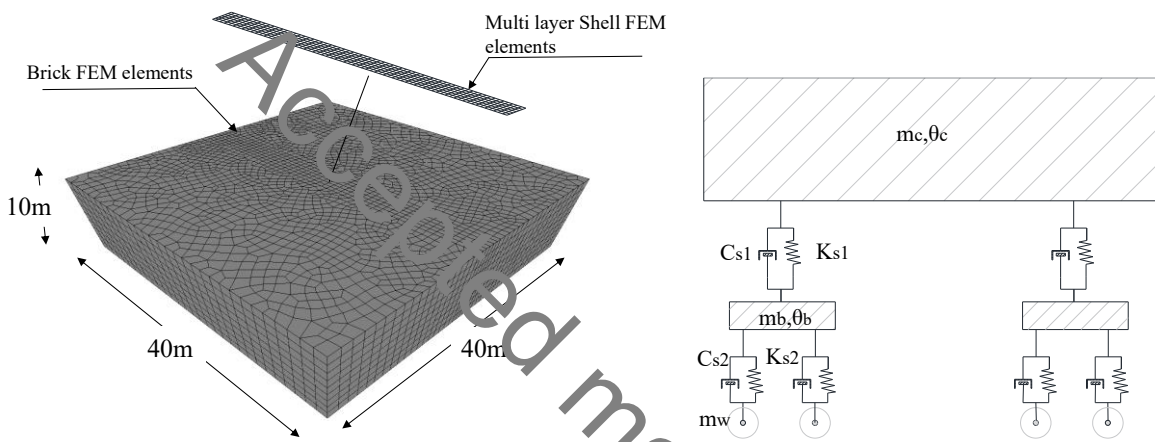


Figure 17. a) ballastless track FEM model b) vehicle model

The measurements at the monitored location along with the response history representing the numerically computed counterpart are illustrated in figure 18a. Additionally, the vertical acceleration of the rail at the monitored location has been calculated from the derivative of a cubic spline function interpolating the measured displacement history. The derived results are compared with the model acceleration in figure 18b.

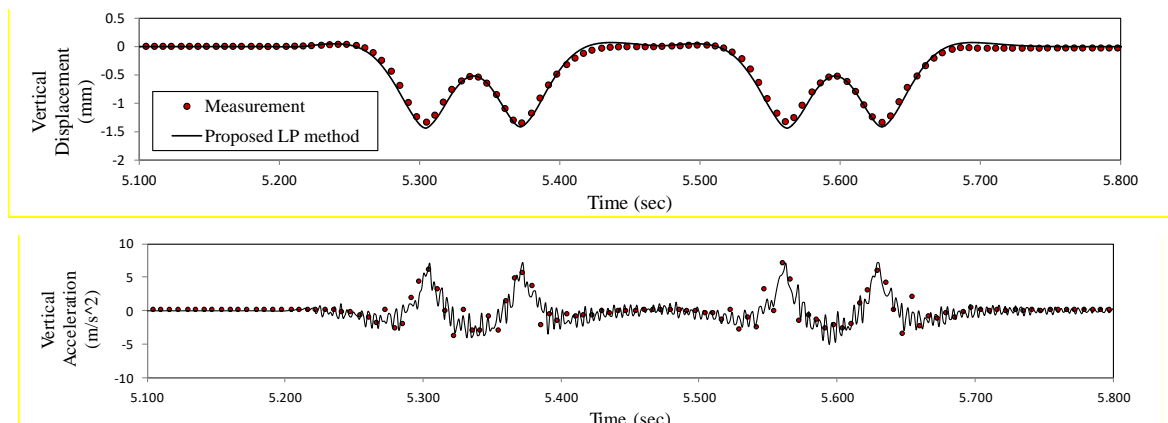


Figure 18. Comparison of numerical and experimental response histories for the rail a) displacement and b) acceleration

Although the train is expected to operate at a constant velocity of 160 km/h, the instantaneous velocity, however, slightly deviates. Thus, the response history has been appropriately modified in order to match a constant instantaneous velocity of 160 km/h.

6. CONCLUSIONS

A step by step reduced order procedure has been proposed for the simulation of the high-speed vehicle-track-subsoil interaction in the time domain. The proposed methodology incorporates a detailed yet computationally efficient representation of wave propagation, refraction and reflection phenomena within the semi-infinite subsoil domain while maintaining the global stability and passivity properties of the vehicle-rail-soil system. The procedure is verified in a numerical case study of a ballasted track founded on a multi-layered soil medium, where the rail response under pre and post critical velocity excitation is evaluated. Complementary verification is accomplished by direct comparison with measured response of an existing monitored ballastless railway track in Germany. The results demonstrate the efficiency of the proposed methodology. Additionally, the proposed method has been implemented by the author in [40] in an extensive sensitivity analysis of coupled vehicle-track-soil systems where rail irregularities have been incorporated in the reduced analysis. Future work is essential to the expansion of the proposed method for the case of inelastic behaviour within the subsoil domain.

ACKNOWLEDGEMENTS

This work was supported by the stakeholders of the Rail Standards and Safety Board (RSSB) research project T1073-2 entitled “Development of a Methodology to Determine Loading Regimes for Track Designers”. This support is gratefully acknowledged. Finally, we would like to thank Dr Charlie Wand and Nicole Krims-Steiner for proofreading the document.

REFERENCES

1. Heckl M, Hauck G, Wettschureck R. Structure-borne sound and vibration from rail traffic. *Journal of Sound and Vibration* 1996; **193**(1): 175–184.
2. Li D, James H, Ted S, Steven C. *Railway Geotechnics*. Taylor & Francis Group,LLC; 2016.
3. Shabana, A. A.; Sugiyama, H.; Zaazaa KE. *Railroad vehicle dynamics. A computational approach*. Boca Raton: CRC Press 2008: 2008.
4. Popp K, SCHIEHLEN W. *ground vehicle dynamics*. . Berlin, Heidelberg: Springer Berlin Heidelberg, 2010. DOI: 10.1007/978-3-540-68553-1978-3-540-68553-1.
5. Kalker JJ. On the Rolling Contact of Two Elastic Bodies in the Presence of Dry Friction. 1967.
6. Vollebregt EAH. *User guide for CONTACT, Rolling and sliding contact with friction*. 2019.
7. Iwnicki S. *Handbook of railway vehicle dynamics*. Taylor & Francis Group,LLC; 2006. DOI: 10.1201/9780849333217.
8. Knothe K, Wu Y. Receptance behaviour of railway track and subgrade. *Archive of Applied Mechanics* 1998; **68**(7–8): 457–470. DOI: 10.1007/s004190050179.

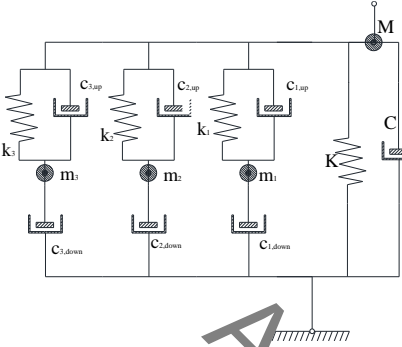
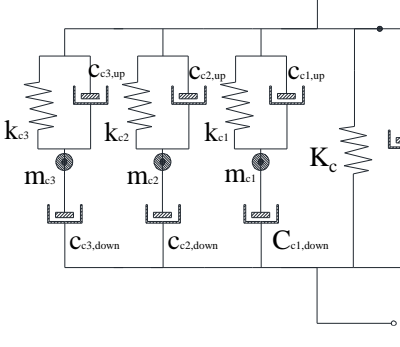
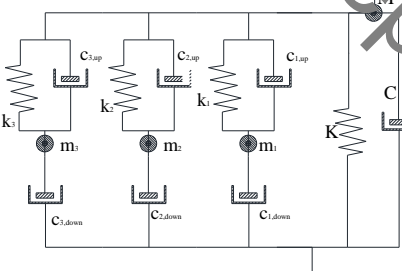
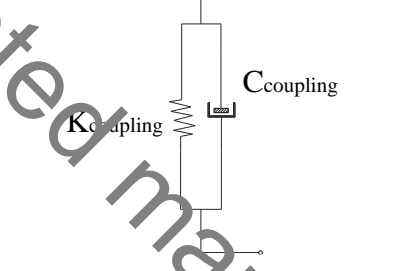
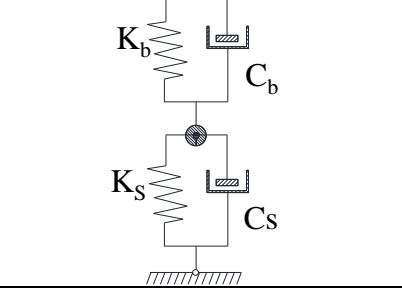
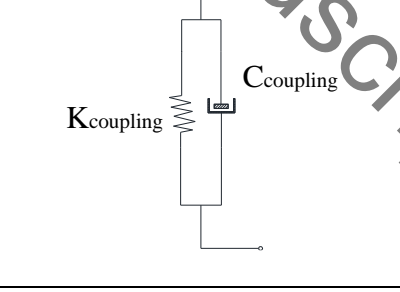
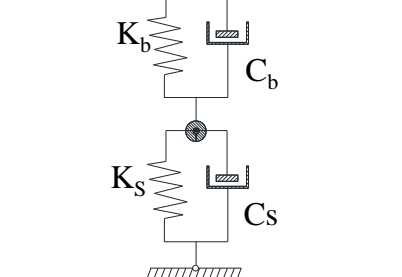
9. Popp K, Kruse H, Kaiser I. Vehicle-Track Dynamics in the Mid-Frequency Range. *Vehicle System Dynamics* 1999; **31**(5–6): 423–464. DOI: 10.1076/vesd.31.5.423.8363.
10. Hall L. Simulations and analyses of train-induced ground vibrations in finite element models. *Soil Dynamics and Earthquake Engineering* 2003; **23**(5): 403–413. DOI: 10.1016/S0267-7261(02)00209-9.
11. Kouroussis G, Verlinden O, Conti C. Free field vibrations caused by high-speed lines: Measurement and time domain simulation. *Soil Dynamics and Earthquake Engineering* 2011; **31**(4): 692–707. DOI: 10.1016/j.soildyn.2010.11.012.
12. Connolly DP, Kouroussis G, Woodward PK, Alves Costa P, Verlinden O, Forde MC. Field testing and analysis of high speed rail vibrations. *Soil Dynamics and Earthquake Engineering* 2014; **67**: 102–118. DOI: 10.1016/j.soildyn.2014.08.013.
13. Kouroussis G, Verlinden O, Conti C. On the interest of integrating vehicle dynamics for the ground propagation of vibrations: the case of urban railway traffic. *Vehicle System Dynamics* 2010; **48**(12): 1553–1571. DOI: 10.1080/00423111003602392.
14. Yang J, Zhu S, Zhai W, Kouroussis G, Wang Y, Wang K, *et al.* Prediction and mitigation of train-induced vibrations of large-scale building constructed on subway tunnel. *Science of the Total Environment* 2019; **668**: 485–499. DOI: 10.1016/j.scitotenv.2019.02.397.
15. Galvín P, Romero A, Domínguez J. Fully three-dimensional analysis of high-speed train–track–soil–structure dynamic interaction. *Journal of Sound and Vibration* 2010; **329**(24): 5147–5163. DOI: 10.1016/j.jsv.2010.06.016.
16. Auersch L. Dynamics of the railway track and the underlying soil: The boundary-element solution, theoretical results and their experimental verification. *Vehicle System Dynamics* 2005; **43**(9): 671–695. DOI: 10.1080/00423110412331307663.
17. Sheng X., Jones C.J.C., Thompson D.J. Prediction of ground vibration from trains using the wavenumber finite and boundary element methods. *Journal of Sound and Vibration* 2006; **293**(3–5): 575–586. DOI: 10.1016/j.jsv.2005.08.040.
18. Wolf J, Somain D. Approximate dynamic model of embedded foundation in time domain. ... *Engineering & Structural Dynamics* 1986; **14**. DOI: 10.1002/eqe.4290140502.
19. Paronesso A, Wolf J. Global lumped-parameter model with physical representation for unbounded medium. *Earthquake Engineering & Structural ...* 1995; **24**(November 1994): 637–654.
20. Saitoh M. Simple model of frequency-dependent impedance functions in soil-structure interaction using frequency-independent elements. *Journal of Engineering Mechanics* 2007; **133**: 1101–1114.
21. Lesgidis N, Kwon OS, Sextos A. A time-domain seismic SSI analysis method for inelastic bridge structures through the use of a frequency-dependent lumped parameter model. *Earthquake Engineering and Structural Dynamics* 2015; **44**(13). DOI: 10.1002/eqe.2573.
22. Lesgidis N, Sextos A, Kwon OS. A frequency-dependent and intensity-dependent macroelement for reduced order seismic analysis of soil-structure interacting systems. *Earthquake Engineering and Structural Dynamics* 2018. DOI: 10.1002/eqe.3063.
23. Wu TX, Thompson DJ. Theoretical Investigation of Wheel/Rail Non-Linear Interaction due to Roughness Excitation. *Vehicle System Dynamics* 2000; **34**(4): 261–282. DOI: 10.1076/vesd.34.4.261.2060.
24. Gerstberger U, Knothe K, Wu Y. Combined Modelling of Discretely Supported Track Models and Subgrade Models — Vertical and Lateral Dynamics. *System Dynamics and Long-Term Behaviour of Railway Vehicles, Track and Subgrade*, vol. 6, Berlin, Heidelberg: Springer Berlin Heidelberg; 2003. DOI: 10.1007/978-3-540-45476-2_15.
25. Kouroussis G, Gazetas G, Anastasopoulos I, Conti C, Verlinden O. Discrete modelling of vertical track-soil coupling for vehicle-track dynamics. *Soil Dynamics and Earthquake Engineering* 2011; **31**(12): 1711–1723. DOI: 10.1016/j.soildyn.2011.07.007.
26. Kouroussis G, Zhu S yang, Olivier B, Ainalis D, Zhai W ming. Urban railway ground vibrations induced by localized defects: using dynamic vibration absorbers as mitigation solution. *Journal of Zhejiang University: Science A* 2019; **20**(2): 83–97. DOI: 10.1631/jzus.A1800651.
27. Koroma SG, Thompson DJ, Hussein MFM, Ntsios E. A mixed space-time and wavenumber-frequency domain procedure for modelling ground vibration from surface railway tracks. *Journal of Sound and Vibration* 2017; **400**: 508–532. DOI: 10.1016/j.jsv.2017.04.015.
28. Khalil HK. *Nonlinear control*. Pearson Higher Ed; 2014.
29. Zhao M, Li H, Du X, Wang P. Time-Domain Stability of Artificial Boundary Condition Coupled with Finite Element for Dynamic and Wave Problems in Unbounded Media. *International Journal of Computational Methods* 2018; **15**(3). DOI: 10.1142/S0219876218500998.
30. Duarte Laudon A, Kwon O, Ghaemmaghami AR. Stability of the time-domain analysis method including a frequency-dependent soil-foundation system. *Earthquake Engineering & Structural Dynamics* 2015; **44**(15): 2737–2754. DOI: 10.1002/eqe.2606.
31. Felippa CA, Park KC, Farhat C. Partitioned analysis of coupled mechanical systems. *Computer Methods in Applied Mechanics and Engineering* 2001; **190**(24–25): 3247–3270. DOI: 10.1016/S0045-7825(00)00391-1.
32. Zadeh L. Optimality and non-scalar-valued performance criteria. *Automatic Control, IEEE Transactions On* 1963; **8**(1): 59–60. DOI: 10.1109/tac.1963.1105511.
33. Coleman TF, Li Y. An Interior Trust Region Approach for Nonlinear Minimization Subject to Bounds. *SIAM Journal on Optimization* 1996; **6**(2): 418–445. DOI: 10.1137/0806023.
34. Gazetas G. Formulas and charts for impedances of surface and embedded foundations. *Journal of Geotechnical Engineering* 1991.
35. Novak M, Mitwally H. Transmitting Boundary for Axisymmetrical Dilation Problems. *Journal of Engineering Mechanics* 1988; **114**(1): 181–187. DOI: 10.1061/(ASCE)0733-9399(1988)114:1(181).
36. Novak M, Nogami T, Aboul-Ella F. Dynamic Soil Reactions For Plain Strain Case. *Journal of the Engineering Mechanics Division*

- 1978; **104**: 953–959.
37. Kennedy J, Eberhart R. Particle swarm optimization. *Neural Networks, 1995 Proceedings, IEEE International Conference On* 1995; **4**: 1942–1948 vol.4. DOI: 10.1109/ICNN.1995.488968.
 38. de Myttenaere A, Golden B, Le Grand B, Rossi F. Mean Absolute Percentage Error for regression models. *Neurocomputing* 2016; **192**: 38–48. DOI: 10.1016/j.neucom.2015.12.114.
 39. Bronsert J. Numerische Modellierung der Fahrzeug-Fahrweg-Wechselwirkung an Eisenbahnfahrwegen und ihre Anwendung im Brückenübergangsbereich. 2017.
 40. Report: Analysis of Coupled Vehicle-Track-Soil Systems, Development of a Methodology to Determine Loading Regimes for Track Designers T1073, RSSB

Accepted manuscript

APPENDIX A

Table I – parameter values, stiffness in (KN/m), damping constant in (KN*s/m), mass in (tn)

Direct component	Coupling component	Parameter values
		<p>Core component: $K=14792.90$, $C=0$, $M=0$ $m_1=32.70$, $m_2=2.17$, $m_3=1.27$ $c_{1,up}=716.73$, $c_{2,up}=0$, $c_{3,up}=97.58$ $c_{1,down}=0$, $c_{2,down}=154$, $c_{3,down}=0$ $k_1=3293$, $k_2=3230$, $k_3=582487$</p> <p>Coupling Component: $K_c=85470$, $C_c=9482^*$, $m_{c1}=6.88$, $m_{c2}=0$, $m_{c3}=6.05$ $c_{c1,up}=6885$, $c_{c2,up}=3169$, $c_{c3,up}=205.06$ $c_{c1,down}=6.00$, $c_{c2,down}=8349$, $c_{c3,down}=4592.94$ $k_{c1}=3752022$, $k_{c2}=46.59$, $k_{c3}=6000264.58$</p>
		<p>Core component: The same as the model above.</p> <p>Coupling Component: $K_{coupling}=14792.90$ $C_{coupling}=0.016$</p>
		<p>Core component: $K_s=14777$, $C_s=853$ $K_b=970563$, $C_b=480$</p> <p>Coupling Component: $K_{coupling}=85630.85$ $C_{coupling}=0.016$</p>
	<p style="text-align: center;">-</p>	<p>Core component: $K_s=72700$, $C_s=853$ $K_b=970563$, $C_b=480$</p>

* cross diagonal terms of Cc dashpot have positive sign instead of conventional negative